Separability of H_2O molecular potential surfaces in hyperspherical coordinates via adiabatic approximation

Jiří Daněk [*] and C. D. Lin [†]
Department of Physics, Kansas State University, Manhattan, Kansas 66506, USA

(Received 2 July 2020; accepted 18 August 2020; published 12 October 2020)

An adiabatic scheme for separation of the three-dimensional (3D) nuclear dynamics on the ground electronic Born-Oppenheimer potential energy surface of an H_2O molecule in hyperspherical coordinates is presented. It is found that the three vibrational modes are weakly coupled and the 3D vibrational wave function can be approximated as a product of three separable functions: one represented by the hyperradius and two by the two hyperangles individually. This framework is then used for investigation of the formation and the role of a saddlelike barrier arising in the two hyperspherical angles that is to moderate the OH + H dissociation process. In order to test the validity of the framework, vibrational states with energies up to 19 500 cm^{-1} are constructed under the assumptions of adiabaticity and separability and compared to full three-dimensional high-precision numerical calculations yielding remarkable correspondence. As a result we present a simple construction scheme for separated molecular vibration states as the first step towards theoretical investigation of laser-driven molecular dynamics of triatomic molecules.

DOI: 10.1103/PhysRevA.102.042809

I. INTRODUCTION

With the rapid development of laser technology, femtosecond and even attosecond experimental techniques in the recent years [1–3], the need for comprehensible theoretical models of molecular vibrational states which take part in the dynamics grows. Although various *ab initio* quantum calculation packages allow fast calculation of normal modes and their frequencies, determination of higher vibrational states and their energies still requires knowledge of the potential energy surface (PES) and solution of full-dimensional time-independent Schrödinger equations. The difficulty owes much to the increasing number of internal degrees of freedom of a molecule which grows as $3N - 5$ for linear molecules and $3N - 6$ for nonlinear molecules, where N is the number of atoms in the molecule. Clearly a full-dimensional quantum mechanical numerical solution is prohibitively complicated. The second complication presents the separability of the vibrational states into modes which is directly connected with a suitable choice of a coordinate system. While quantum mechanical numerical solutions can be, in principle, obtained in any coordinates, the states may not exhibit any clear nodal structure required for unambiguous identification of modes and assignment of quantum numbers.

Separability of vibrational modes can significantly simplify dynamical nuclear problems, e.g., due to symmetry reasons. Standard and attractive approximation for complex molecules is to freeze all the degrees of freedom except for one interatomic pair or an angle between two such pairs. This avoids the treatment of a multidimensional surface and the analysis of the dynamics can be dramatically simplified. On the other hand, such simplification may occur in several distinct regions of the multidimensional potential surface only, such that connecting such regions in a time-dependent way is needed. Before such an approach can be established, however, it is critical that one can identify the circumstance where dynamics in a multidimensional potential surface can be simplified, preferably as separable components. For this purpose, we aim at examining the ground-state potential surface of water molecules (H_2O), with the goal of identifying the separability of the nuclear degrees of freedom.

Over the years, several models for the nuclear vibrations of H_2O have been formulated. The initial attempt assumed only small displacements of atoms from their equilibrium position so that the molecular potential expanded at the equilibrium could be diagonalized alongside with the kinetic term, giving rise to the well-known normal modes (see, e.g., Ref. [4]). The normal modes, however, experience various mixings: Fermi [5] at lower energies and Darling-Dennison [6] at high energies. Moreover, the anharmonicity of the potential had to be taken into account by correcting terms [7]. Later it was shown that the so-called local-mode model provides an overall better fit to vibration energies (see, e.g., Ref. [8] and references therein). Nevertheless, the local mode description fails for the lower vibration states due to the relatively small mass of the oxygen atom and yields a good agreement only from the fourth polyad on [9]. Moreover, for water molecules not all normal modes get washed out due to the Darling-Dennison mixing and some survive alongside the local modes up to high energies [10].

Hyperspherical modes offered an alternative to the two presented types of modes, giving rise to various methods for hyperspherical mode determination based on adiabatic approximation (e.g., see Ref. [11] and references therein) or

[*] danekj@phys.ksu.edu
[†] cdlin@phys.ksu.edu

on assumption of mode separability in the self-consistent field approach [12]. Selective dissociation through hyperspherical modes was investigated in Refs. [13–16] and adiabatic separability of stretching and bending modes in Radau and valence coordinates was addressed in Ref. [17].

A new era in the theoretical spectroscopy of H_2O came with precise *ab initio* calculations of molecular PESs [18–26] which allowed one to calculate line lists for H_2O with high precision up to 41 000 cm^{-1} and $J = 72$ [27]. These listed PESs either are constructed completely from *ab initio* calculations or use them as a starting surface which then is fine-morphed to fit available spectroscopic data. As we have already mentioned, both normal-mode- and local-mode-based methods offer unique insight into the internal dynamics of molecules.

In this work, we investigate the separability of the PES of the H_2O molecule from Ref. [28] in hyperspherical coordinates [29]. We use the adiabatic approximation to separate the motion associated with the symmetrical stretch from the motions in two hyperangles associated with bending and antisymmetric stretching modes. Further, we separate the motion in the two hyperangular coordinates, resulting eventually in three independent one-dimensional (1D) Schrödinger equations. As one of our results, we reconstructed the full 3D states within our separability assumption and benchmark the found energies against high-precision numerical results from Ref. [30]. The goal of this work is to construct separated vibration states with trivially given symmetry and quantum numbers reasonably resembling the real vibration states and energies with the lowest effort possible. We regard the development of such a framework as an essential step towards theoretical investigation of strong-field processes in triatomic molecules. Especially, we hope that the hyperspherical coordinates will help us in the future to shed light on the selective dissociation limit for water isotopomers (e.g., HOD) as they lose their molecular symmetry. In such a case, the bond between the diatomic remnants will play a crucial role and is well described within one of the sets which we introduce later.

The paper is structured as follows. In Sec. II we introduce the hyperspherical coordinates via three different sets of Jacobi coordinates and show how the H_2O molecule and the PES behave in these coordinates. Further in that section, we transform the Hamiltonian in hyperspherical coordinates. We further introduce the grand angular momentum operator and analyze the modes given in hyperspherical coordinates. The adiabatic approximation and decomposition of the 3D Hamiltonian in hyperspherical coordinates into two parts is discussed in Sec. III. Moreover, all nonadiabatic correction terms are derived and a way is shown how to solve the adiabatic 2D Hamiltonian with B-spline basis functions. In Sec. IV we discuss the main novelty of this work: possible separability of the PES in the current hyperspherical coordinates. In the course of this action the 2D vibration wave functions are constructed in the separability approximation and analyzed. Their role in the OH + H dissociation process is also discussed. The full separability of the 3D PES in all three hyperspherical coordinates is addressed in Sec. V where the total energies are calculated in the adiabatic approximation neglecting nonadiabatic corrections and compared to full 3D numerical calculations. Finally, the results are discussed and concluded in Sec. VI. A deeper analysis of the atomic displacements associated with the hyperspherical modes is provided in the Appendix. Atomic units are used throughout the text unless stated otherwise.

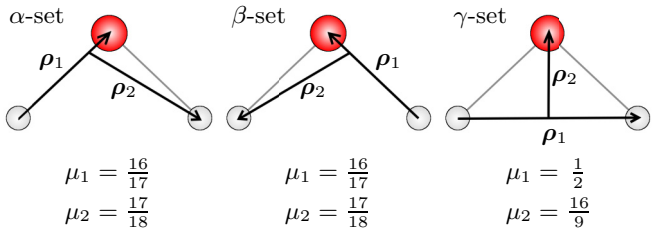

FIG. 1. Demonstration of the three ways for defining Jacobi vectors with corresponding reduced masses μ_1 and μ_2.

II. FORMULATION IN HYPERSPHERICAL COORDINATES

A. Mass-scaled hyperspherical coordinates

Internal degrees of freedom for the triatomic H_2O molecule can be described by Jacobi vectors in three different ways as shown in Fig. 1. The first Jacobi vector $\boldsymbol{\rho}_1$ always points from one atom to another, whereas the second vector $\boldsymbol{\rho}_2$ points from the center-of-mass of the two atoms to the third one.

Further, it is common to introduce mass-weighted Jacobi coordinates as

$$\boldsymbol{\xi}_1 = \sqrt{\frac{\mu_1}{\mu}}\boldsymbol{\rho}_1, \qquad \boldsymbol{\xi}_2 = \sqrt{\frac{\mu_2}{\mu}}\boldsymbol{\rho}_2, \tag{1}$$

with an arbitrary parametric mass μ and the reduced masses

$$\begin{aligned} \mu_1 &= \frac{m_a m_b}{m_a + m_b}, \\ \mu_2 &= \frac{(m_a + m_b)m_c}{m_a + m_b + m_c}, \end{aligned} \tag{2}$$

where indices a, b, and c depend on the set of Jacobi coordinates. The masses in μ_1 are the masses of the atoms connected by $\boldsymbol{\rho}_1$, and the third remaining mass in μ_2 is the mass of the last atom.

The hyperspherical coordinates can be defined in several ways but we follow the definition from [29] yielding

$$\begin{aligned} R &= \sqrt{\xi_1^2 + \xi_2^2}, \\ \phi &= \operatorname{atan}\frac{\xi_2}{\xi_1}, \\ \theta &= \operatorname{acos}\frac{\boldsymbol{\xi}_1 \cdot \boldsymbol{\xi}_2}{\xi_1 \xi_2}. \end{aligned} \tag{3}$$

Although the values of ϕ and θ vary when transforming between the sets, the value R is identical for all three sets. Configurations of the molecule with respect to the angles ϕ and θ are shown in Fig. 2. The figures are carried out for a constant value of R but are valid for any value of the hyperradius. The hyperradius is connected only to the overall size of the molecule and does not change the internal angles nor the ratio between the two bond lengths used for determination of the dissociation regions. In this work we set $\mu = \mu_2$ from

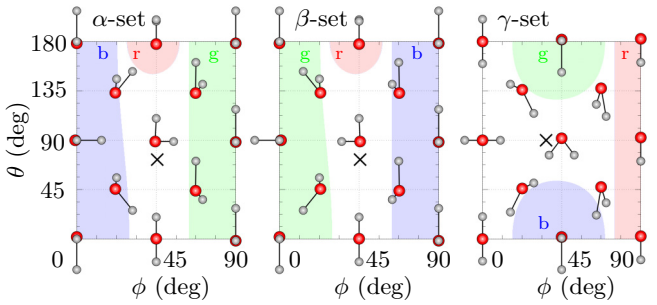

FIG. 2. Configuration of the molecule (HOH) at a constant hyperradius R with respect to hyperspherical coordinates ϕ and θ and the choice of set. The second Jacobi vector is always oriented along the θ axis. The position of the global minimum is marked with black cross. The shaded regions indicate which atom is the furthest from the others: in the blue region (labeled as b) it is the first hydrogen (H + OH), in red region (labeled as r) it is the oxygen (H_2 + O), and in green region (labeled as g) it is the second hydrogen (HO + H).

the γ set, which sets the minimum of the potential to hyperradius $R = 1.881$ a.u. and to hyperangles $\phi = 45.52^\circ$ and $\theta = 72.32^\circ$ for both the α set and the β set and to hyperangles $\phi = 36.15^\circ$ and $\theta = 90^\circ$ for the γ set. The global minimum is marked by a cross in each of the panels in Fig. 2.

The PES of the H_2O molecule possesses only one global minimum, which is also called equilibrium. Nevertheless, it is of interest to have a look at the position of the minimum in each slice of the PES with respect to the hyperradius as we do in Fig. 3. The global minimum is marked by a black cross and lies on the purple curve which marks the position of the minimum of the 2D PES slice of constant R. Remarkably, the position of the minimum manifests a split starting at $R \approx 2.4$. Since the α set does not exploit the molecular symmetry, the split minima are located at distinct hyperangles ϕ and θ as the figure shows. This is different for the γ set, which reflects the molecular symmetry. In this set, both split minima are located at the same value of hyperangle ϕ and their position in hyperangle θ respects the axis of symmetry $\theta = 90^\circ$. We discuss later in the text how this bifurcation point is connected to two dissociation channels OH + H.

B. Molecular Hamiltonian

The molecular Hamiltonian in Cartesian coordinates $\mathbf{x}_i$ of the ith nucleus yields

$$\hat{H} = \sum_{i=1}^{3} -\frac{1}{2m_i}\nabla^2(\mathbf{x}_i) + V, \tag{4}$$

with the potential V accounting for the electronic energy and the nuclear repulsion energy. For three atoms, in Jacobi coordinates, the rovibrational Hamiltonian simplifies to [31,32]

$$\hat{H}' = \hat{K}_{\rm vr} + \hat{K}_{\rm v} + V(\rho_1, \rho_2, \theta), \tag{5}$$

where

$$\begin{aligned}
\hat{K}_{\rm vr} &= \frac{1}{2}\left[\frac{1}{\mu_2\rho_2^2}\left(\Pi_x^2 + \Pi_y^2\right) + \left(\frac{\operatorname{cosec}^2\theta}{\mu_1\rho_1^2} + \frac{\cot^2\theta}{\mu_2\rho_2^2}\right)\Pi_z^2 + \frac{\cot\theta}{\mu_2\rho_2^2}\left(\Pi_x\Pi_z + \Pi_z\Pi_x\right)\right] - \frac{i}{\mu_2\rho_2^2}\left(\frac{\partial}{\partial\theta} + \frac{\cot\theta}{2}\right)\Pi_y, \\
\hat{K}_{\rm v} &= -\frac{1}{2\mu_1\rho_1^2}\frac{\partial}{\partial\rho_1}\left(\rho_1^2\frac{\partial}{\partial\rho_1}\right) - \frac{1}{2\mu_2\rho_2^2}\frac{\partial}{\partial\rho_2}\left(\rho_2^2\frac{\partial}{\partial\rho_2}\right) - \frac{1}{2}\left(\frac{1}{\mu_1\rho_1^2} + \frac{1}{\mu_2\rho_2^2}\right)\frac{1}{\sin\theta}\frac{\partial}{\partial\theta}\left(\sin\theta\frac{\partial}{\partial\theta}\right).
\end{aligned} \tag{6}$$

The terms $\hat{K}_{\rm vr}$ and $\hat{K}_{\rm v}$ represent the rovibrational part and the vibration part of the Hamiltonian, respectively. The quantities Π_α are the total angular momentum operators which depend on the Euler angles in such a way that the components of the total angular momentum in $\boldsymbol{\rho}_i$ can be obtained from matrix multiplication:

$$\mathbf{L} = -\mathbf{C}\boldsymbol{\Pi}. \tag{7}$$

The volume element for the internal coordinates yields $dV = \rho_1^2\rho_2^2\sin\theta d\rho_1 d\rho_2 d\theta$ and for the Euler angle part it depends on the sine of the second Euler angle. For further details about Jacobi coordinates in the embedded body frame, see Ref. [31].

From now on, we concentrate only on the vibrational kinetic term of the Hamiltonian $\hat{K}_{\rm v}$ which yields the following in hyperspherical coordinates:

$$\hat{K}_{\rm v} = -\frac{1}{2\mu}\frac{\partial^2}{\partial R^2} + \frac{\Lambda^2 - \frac{1}{4}}{2\mu R^2}, \tag{8}$$

with the squared grand angular momentum operator

$$\Lambda^2 = -\frac{\partial^2}{\partial\phi^2} - \frac{1}{\sin^2\phi\cos^2\phi\sin\theta}\frac{\partial}{\partial\theta}\left(\sin\theta\frac{\partial}{\partial\theta}\right). \tag{9}$$

Let us note that in the calculation the wave function was rescaled by a factor of $R^{5/2}\sin\phi\cos\phi$ and the volume element now becomes $dV = \sin\theta dR d\phi d\theta$. Let us also remark that transformation of the wave function from hyperspherical to Cartesian coordinates can be performed simply by removing the scaling factor.

C. Hyperspherical and normal modes

It is reasonable to exploit the trivial symmetry of the water molecule and connect the two hydrogen atoms with the first Jacobi vector, which we call the γ set for conventional reasons. Reduced masses in such a case yield

$$\mu_1 = \frac{m_{\rm H}}{2}, \quad \mu_2 = \frac{4\mu_1 m_{\rm O}}{4\mu_1 + m_{\rm O}}. \tag{10}$$

The Jacobi vectors can be fixed in the embedded body frame following Ref. [31] as

$$\boldsymbol{\rho}_1 = \rho_1\begin{pmatrix}\sin\theta\\0\\\cos\theta\end{pmatrix}, \quad \boldsymbol{\rho}_2 = \rho_2\begin{pmatrix}0\\0\\1\end{pmatrix}, \tag{11}$$

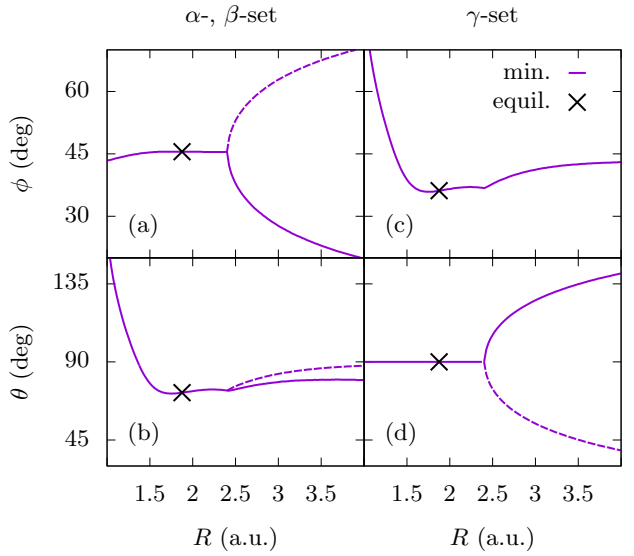

FIG. 3. Position of the minima in slices of the potential, i.e., $V(R = \text{const.}, \phi, \theta)$, in hyperspherical coordinates with respect to R are projected and marked with magenta lines for the α and β sets in panels (a) and (b) and for the γ set in panels (c) and (d). The position of the global minimum is marked with a black cross. We can see that the minimum of the potential splits at $R \approx 2.4$ and two minima are created (denoted with solid and dashed lines). In the α and β sets, both minima are located at different hyperangles. In the γ set, the two minima are located at the same hyperangle ϕ and in hyperangle θ they respect the symmetry axis $\theta = 90°$. Let us also remark that the two minima interchange under transformations between the α and β sets.

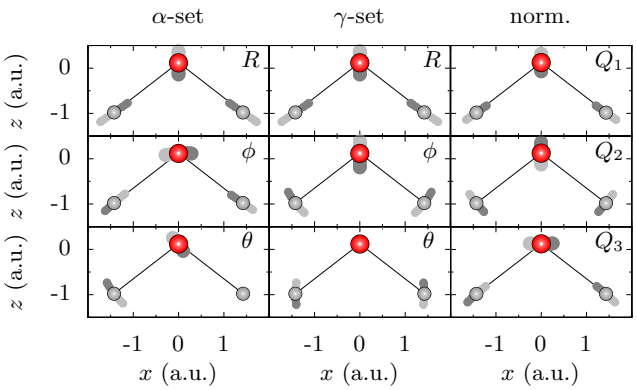

FIG. 4. Visualization of hyperspherical modes in the α and γ sets, and normal modes, as change in the positions of individual atoms. The center-of-mass of the molecule is fixed at the origin and normal coordinates Q_1, Q_2, and Q_3 and hyperspherical coordinates R, ϕ, and θ execute oscillation over one whole period. The positions of the atoms during the first half-period are shown with light gray and for the second half-period with dark gray. The displacements of oxygen atom are exaggerated by a factor of 10. For more details see the text.

meaning that the oxygen atom, the center-of-mass of the molecule, and the center-of-mass of the two hydrogens lie on the z axis.

One could ask: how do the changes in the hyperspherical coordinates R, ϕ, and θ manifest? We carried the change of the positions of the atoms connected with the hyperspherical coordinates R, ϕ, and θ for the α and γ sets along with normal coordinates (taken from Ref. [33]) in Fig. 4. We can identify oscillations in Q_1 and R as symmetric stretching, in Q_2 and ϕ (γ set) as bending, and in Q_3 and ϕ (α-set) as asymmetric stretching. The mode in hyperangle θ (γ set) reflects the symmetry of the asymmetric bond-stretching in Q_3, but does not seem to be a linear combination of the three normal modes as the position of the oxygen atom does not change. Let us note that the modes in Q_2 and ϕ (γ set), although similar looking, are not identical and, moreover, act in opposite directions, since for increasing Q_2 the molecule straightens, whereas for increasing ϕ the molecule bends more. To conclude this comparison we note that the modes in Q_3 and ϕ (α set) are not identical either.

In addition, we have analyzed the atomic displacements in the γ set of hyperspherical coordinates analytically and the results are given in the Appendix.

III. ADIABATIC APPROXIMATION IN HYPERSPHERICAL COORDINATES

A. The Born-Oppenheimer approximation

In order to simplify Eq. (5), we apply the well-known Born-Huang expansion of the wave function $\psi(R, \phi, \theta)$ in the form

$$\psi(R, \phi, \theta) = \sum_{\nu} F_{\nu}(R)\Phi_{\nu}(R, \phi, \theta). \tag{12}$$

When we insert the expansion into Eq. (5) with the vibrational term from Eq. (8) and assume adiabatic behavior with respect to the R coordinate, we arrive at two coupled equations:

$$\left(\frac{\Lambda^2 - 1/4}{2\mu R^2} + V(R, \phi, \theta)\right)\Phi_{\nu}(R, \phi, \theta) = U_{\nu}(R)\Phi_{\nu}(R, \phi, \theta), \tag{13}$$

$$\left(-\frac{1}{2\mu}\frac{d^2}{dR^2} + U_{\nu}(R)\right)F_{\nu n}(R) = E_{\nu n}F_{\nu n}(R), \tag{14}$$

where index ν represents the vibrational quantum number of the 2D wave function $\Phi_{\nu}(R, \phi, \theta)$ with energy $U_{\nu}(R)$ on a slice of the potential, i.e., $V(R = \text{const.}, \phi, \theta)$. Later we address the fact that the energies of two distinct vibrational states can become degenerate and even cross with changing R. Index n stands for the vibrational quantum number of the 1D wave function $F_{\nu n}(R)$ on the 1D potential curve given by $U_{\nu}(R)$ with the fixed value ν. The energy $E_{\nu n}$ then represents the total vibrational energy of the molecule under the adiabatic approximation applied on the nuclear coordinates. We can treat R as a parameter in the first equation and as a coordinate in the second equation. Let us stress that all nonadiabatic

terms in the second equation are omitted so it is equivalent to the Born-Oppenheimer approximation for the "slow" coordinate R. It is known that such an approximation leads to determination of the lower bound on the energy levels [34]. However the upper bound is usually closer to the real result [35] and can be obtained by reintroduction of the nonadiabatic term

$$W_{\nu\nu}(R) = -\frac{1}{2\mu}\langle\Phi_\nu(R)|\frac{d^2}{dR^2}|\Phi_\nu(R)\rangle \tag{15}$$

into the round bracket on the left-hand side of Eq. (14) [34]. The bra–ket stands for integration over the hyperangles ϕ and θ.

Let us also note that the energies $E_{\nu n}$ generally do not correspond to nuclear vibrational energies on the 3D adiabatic PES $V(R,\phi,\theta)$, unless the vibrational modes in R and (ϕ,θ) truly separate and all nonadiabatic corrections and couplings vanish, e.g., due to a proper choice of coordinate system. In such case, the energies $E_{\nu n}$ would correspond to the full 3D nuclear vibrational energies in the sense of the Born-Oppenheimer approximation separating electronic and nuclear motion.

B. Nonadiabatic coupling terms

Equations (13) and (14) are obtained by assuming that the nonadiabatic terms are negligible, thus leading to the conclusion that the various states $F_{\nu n}(R)$ do not interact. If the nonadiabatic couplings are included, the full equation, Eq. (14), would take the following form:

$$\left(-\frac{1}{2\mu}\frac{d^2}{dR^2} + U_\nu(R) + W_{\nu\nu}(R) - E_\nu\right)F_\nu(R) = -\sum_{\rho\neq\nu}\left(W_{\nu\rho}(R) + 2V_{\nu\rho}(R)\frac{d}{dR}\right)F_\rho(R), \tag{16}$$

where

$$V_{\nu\rho}(R) = -\frac{1}{2\mu}\langle\Phi_\nu(R)|\frac{d}{dR}|\Phi_\rho(R)\rangle, \tag{17}$$

$$W_{\nu\rho}(R) = -\frac{1}{2\mu}\langle\Phi_\nu(R)|\frac{d^2}{dR^2}|\Phi_\rho(R)\rangle. \tag{18}$$

The Hamiltonian can be decomposed into two terms:

$$H^{(1D)} = H^{(1D)}_{\text{diag.}} + H^{(1D)}_{\text{coupl.}}. \tag{19}$$

The diagonal Hamiltonian has the following form:

$$H^{(1D)}_{\text{diag.}\,\nu\nu} = -\frac{1}{2\mu}\frac{d^2}{dR^2} + U_\nu + W_{\nu\nu}(R), \tag{20}$$

and the nonadiabatic couplings can be written as

$$H^{(1D)}_{\text{coupl.}} = \begin{pmatrix} 0 & W_{12}(R) + 2V_{12}(R)\frac{d}{dR}\cdots \\ W_{21}(R) + 2V_{21}(R)\frac{d}{dR} & 0 \quad \ddots \\ \vdots \quad \ddots & \ddots \end{pmatrix}. \tag{21}$$

C. Solving the 2D angular Schrödinger equation with 2D *B*-splines

Equation (13) can be solved trivially over some real 2D basis set. For this purpose we decided to use 2D B-splines of some order k, chosen to be the same in both dimensions. Then, the wave function can be decomposed as

$$\Phi_\nu(R,\phi,\theta) = \sum_n c_{\nu n}(R)B_n(\phi,\theta), \tag{22}$$

where $B_n(\phi,\theta)$ is the nth 2D B-spline and the coefficients $c_{\nu n}(R)$ are R-dependent constants. The index n represents a unique product of two 1D B-splines of order k constructed on grid of N_ϕ points in one dimension and N_θ points in the other (see, e.g., Ref. [36]). We have chosen $k = 6$ and $N_\phi = 46$ and $N_\theta = 91$.

In the B-spline representation, Eq. (13) yields

$$\sum_n H^{(2D)}_{n'n}(R)c_{\nu n}(R) = \sum_n I_{n'n}c_{\nu n}(R), \tag{23}$$

with the Hamiltonian and overlap matrices as follows:

$$H^{(2D)}_{n'n} = \langle B_{n'}(\phi,\theta)|\hat{H}_{2D}|B_n(\phi,\theta)\rangle,$$
$$I_{n'n} = \langle B_{n'}(\phi,\theta)|B_n(\phi,\theta)\rangle. \tag{24}$$

When we substitute for the grand angular momentum operator from Eq. (9) into Eq. (13), we can evaluate the matrix elements of the angular Hamiltonian as

$$H^{(2D)}_{n'n} = \iint d\phi d\theta \sin\theta B_{n'}\left(V - \frac{1}{8\mu R^2}\right)B_n + \frac{1}{2\mu R^2}\iint d\phi d\theta \sin\theta\left(\frac{\partial B_{n'}}{\partial\phi}\frac{\partial B_n}{\partial\phi} + \frac{1}{\sin^2\phi\cos^2\phi}\frac{\partial B_{n'}}{\partial\theta}\frac{\partial B_n}{\partial\theta}\right), \tag{25}$$

where we applied the boundary conditions $\psi(R,0,\theta) = \psi(R,\pi/2,\theta) = 0$ and $\partial\psi/\partial\theta = 0$ at $\theta = 0$ and π. The overlap matrix can be evaluated simply as

$$I_{n'n} = \iint d\phi d\theta \sin\theta B_{n'}B_n. \tag{26}$$

The diagonalization of this symmetric generalized eigenvalue problem can be done by standard packages (e.g., LAPACK for FORTRAN). The energies U_ν carried out for $R = 1.88$ a.u. are presented in Table I. In this table, quantum numbers ν_ϕ and ν_θ are assigned from the nodal structure. Take U_1 and U_3 as the elementary quanta, it can be seen that the 2D eigenvalues are well approximated by $E_{\nu_\phi,\nu_\theta} = \nu_\phi U_1 + \nu_\theta U_3$.

IV. SEMISEPARABILITY OF THE POTENTIAL IN HYPERSPHERICAL COORDINATES

Normal vibration modes of the water molecule are based on the strict assumption that the potential is separable in the normal coordinates, for example, at least at the equilibrium position, and that vibrational states are independent and quantized with unique quantum numbers and unique energies. As we discuss further, this is not true for highly excited states. Nevertheless, such a simple picture is not far from reality

TABLE I. Analysis of the separation of the potential at $R = 1.88$. We compare the quantized energies constructed via $E_{\nu_\phi,\nu_\theta} = \nu_\phi U_1 + \nu_\theta U_3$ with the calculated energies U_ν of 2D Eq. (13). The overall small relative difference indicates that the potential behaves like being separable in the two hyperangles.

ν	ν_ϕ	ν_θ	E_{ν_ϕ,ν_θ} (cm^{-1})	U_ν (cm^{-1})	Rel. diff. (%)
0	0	0	0	0	—
1	1	0	1634.3	1634.3	—
2	2	0	3268.7	3238.2	0.9
3	0	1	4111.9	4111.9	—
4	3	0	4903.0	4803.7	2.1
5	1	1	5746.3	5770.1	0.4
6	4	0	6537.4	6320.3	3.4
7	2	1	7380.6	7397.6	0.2
8	5	0	8171.7	7770.9	5.2
9	0	2	8223.8	8368.9	1.7
10	3	1	9014.9	8986.8	0.3
11	6	0	9806.1	9122.8	7.5
12	1	2	9858.2	10050.8	1.9
13	7	0	11440.4	10343.4	9.6
14	4	1	10649.3	10527.6	1.1
15	8	0	13074.8	11537.5	13.3
16	2	2	11492.5	11701.7	1.8
17	5	1	12283.6	12003.9	2.3
18	0	3	12335.7	12763.8	3.4
19	9	0	14709.1	12874.7	14.2
20	3	2	13126.9	13314.4	1.4

and this picture helps us to gain insight into the behavior of molecular dynamics.

We have already separated the potential into hyperradial and hyperangular parts in our adiabatic approach: can the equivalent of the three normal modes occur also in the hyperspherical approach?

The answer is not obvious since the grand angular momentum operator Λ^2 from Eq. (9) is not separable in the hyperangles. Nevertheless, we can use a small trick if we assume separability of the 2D wave function with the parameter R and the quantum numbers ν_ϕ and ν_θ in the form

$$\tilde{\Phi}_{\nu_\phi,\nu_\theta}(R,\phi,\theta) = \Phi_{\nu_\phi}(R,\phi)\Theta_{\nu_\theta}(R,\theta). \tag{27}$$

Such a separable form would yield the approximate total 2D energy as

$$\tilde{U}_{\nu_\phi,\nu_\theta} = U_{\nu_\phi} + U_{\nu_\theta}. \tag{28}$$

This trick comes in handy when separation of the grand angular momentum operator along with the molecular potential $V(R,\phi,\theta)$ at the minimum of the potential $(\phi_{\min},\theta_{\min})$ for a given R is set by

$$\begin{aligned}
&\left(\frac{\Lambda_\phi^2 - 1/8}{2\mu R^2} + V(R,\phi,\theta_{\min}) - \frac{1}{2}V(R,\phi_{\min},\theta_{\min})\right)\Phi_{\nu_\phi}(R,\phi) \\
&\quad = U_{\nu_\phi}\Phi_{\nu_\phi}(R,\phi), \\
&\left(\frac{\Lambda_\theta^2 - 1/8}{2\mu R^2} + V(R,\phi_{\min},\theta) - \frac{1}{2}V(R,\phi_{\min},\theta_{\min})\right)\Theta_{\nu_\theta}(R,\theta) \\
&\quad = U_{\nu_\theta}\Theta_{\nu_\theta}(R,\theta),
\end{aligned} \tag{29}$$

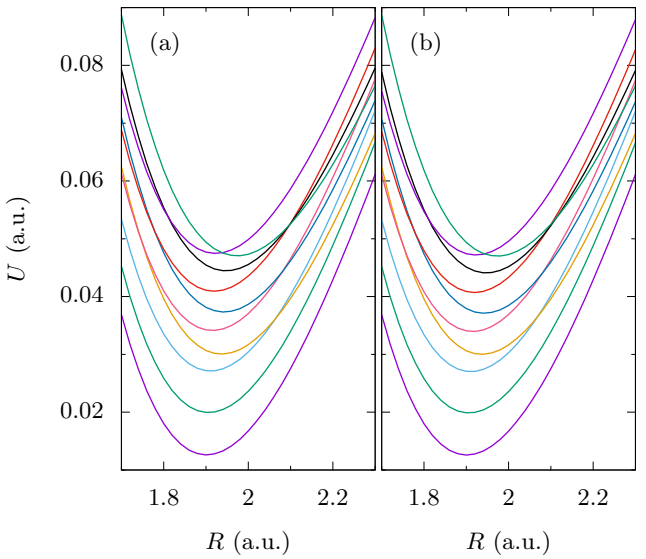

FIG. 5. Adiabatic PECs $U_\nu^{(2D)}$ obtained by solving Eq. (13) with the 2D B-spline basis set are shown in panel (a) and PECs $\tilde{U}_{\nu_\phi,\nu_\theta}$ obtained by separable approximation are plotted in panel (b).

where the separated grand angular operators yield

$$\begin{aligned}
\Lambda_\phi^2 &= -\frac{\partial^2}{\partial\phi^2}, \\
\Lambda_\theta^2 &= -\frac{1}{\sin^2\phi_{\min}\cos^2\phi_{\min}\sin\theta}\frac{\partial}{\partial\theta}\left(\sin\theta\frac{\partial}{\partial\theta}\right).
\end{aligned} \tag{30}$$

Let us note that the quantities obtained within separability approximation are marked with a tilde.

Although this separation may seem arbitrary, it is well founded by the quantization of the 2D wave functions $\Phi_\nu(R,\phi,\theta)$ in the quantum numbers ν_ϕ and ν_θ as we can see in Table I.

This also explains why the resulting potential energy curves (PEC) $\tilde{U}_{\nu_\phi,\nu_\theta}$ are very close to the curves obtained by full 2D calculations (calculated with a B-spline basis set) [see Figs. 5(a) and 5(b)]. Not only is the order of the curves in $U_\nu^{(2D)}$ and $\tilde{U}_{\nu_\phi,\nu_\theta}$ identical, but also the positions of all curve crossings. The exact numerical values at $R = 1.88$ for these two calculations can be found in Table II.

A. Reconstructing $\tilde{\Phi}(\phi,\theta)$

The huge advantage of having two 1D Schrödinger equations instead of one 2D equation is the speed of calculation. The other great advantage is the trivial organization of the eigenstates. The 1D eigenstates in each dimension are quantized with the corresponding quantum number ν_ϕ or ν_θ. Energies of these 1D states increase monotonically with the increasing quantum number, and similar states in various R slices of the PES can be easily assigned. Such organization also applies for the constructed 2D wave functions $\tilde{\Phi}_{\nu_\phi,\nu_\theta}$. This is not true for the adiabatic 2D states as there are slices where quasiseparability breaks down and nodes in the two dimensions cannot be distinguished. Trying to connect the 2D adiabatic states in neighboring slices via their overlap, $\langle\Phi_\nu(R_i)|\Phi_{\nu'}(R_{i+1})\rangle$, works for the four lowest-lying states

TABLE II. Comparison of energies at $R = 1.88$ a.u. for low-lying states obtained by several methods as discussed in the text. Energies $\tilde{U}_{\nu_\phi,\nu_\theta}$ are determined under the assumption of separable potential while $U_\nu^{(2D)}$ are true adiabatic potentials. The diagonal full Hamiltonian matrix element $\tilde{H}^{(full)}_{(\nu)(\nu)}$ gives the energy of the 2D Hamiltonian if the eigenstates are separable. $\tilde{E}^{(full)}_{(\nu)}$ gives the energy after diagonalization of 2D Hamiltonian with the basis constructed by the separable states. Thus the separable states can serve as a diabatic basis set.

ν	ν_ϕ	ν_θ	$\tilde{U}_{\nu_\phi,\nu_\theta}$	$\tilde{H}^{(full)}_{(\nu)(\nu)}$	$\tilde{E}^{(full)}_{(\nu)}$	$U_\nu^{(2D)}$
0	0	0	0.01280	0.01287	0.01283	0.01283
1	1	0	0.02020	0.02047	0.02027	0.02027
2	2	0	0.02746	0.02808	0.02758	0.02758
3	0	1	0.03152	0.03174	0.03156	0.03156
4	3	0	0.03455	0.03578	0.03472	0.03472
5	1	1	0.03892	0.03977	0.03912	0.03912
6	4	0	0.04142	0.04384	0.04163	0.04163
7	2	1	0.04618	0.04813	0.04653	0.04653
8	5	0	0.04801	0.05322	0.04830	0.04823
9	0	2	0.05093	0.05130	0.05096	0.05096

only, while for higher-lying states they cannot be connected correctly via this method through a split of the potential at $R \approx 2.43$. Further challenge is posed at $R \approx 3.19$ a.u. where the full 2D eigenfunctions also lack clear nodal structure in each dimension, making the connection rather nontrivial.

The natural thing to ask is: how precise are the 2D wave functions constructed by two 1D wave functions obtained from the separation method in Eq. (29)? To answer this question we can use two ways. On one hand, we can evaluate the overlap between the constructed states and the real 2D states:

$$a_{i,(\nu)} = \langle \Phi_i | \tilde{\Phi}_{(\nu)} \rangle, \tag{31}$$

where hyperindex (ν) represents one particular combination of the quantum numbers ν_ϕ and ν_θ. The assignment of ν_ϕ and ν_θ to the hyperindex ν follows the scheme from Table II (for example, if $\nu = 6$ then $\nu_\phi = 4$ and $\nu_\theta = 0$). We show the projections in Table III. On the other hand, we can evaluate the full Hamiltonian matrix

$$\tilde{H}^{(full)}_{(\nu_1)(\nu_2)} = \langle \tilde{\Phi}_{(\nu_1)} | \frac{\Lambda^2 - 1/4}{2\mu R^2} + V | \tilde{\Phi}_{(\nu_2)} \rangle, \tag{32}$$

with hyperindices (ν_1) and (ν_2). The more the diagonal elements of the matrix $\tilde{H}^{(full)}_{(\nu)(\nu)}$ deviate from the corresponding energy $\tilde{U}_{\nu_\phi,\nu_\theta}$, the more the constructed wave functions deviate from the true adiabatic 2D wave functions. Such deviations start to become prominent for the 7th ($\nu = 6$) and 9th ($\nu = 8$) energy levels. The discrepancy can be attributed to the high quantum number ν_ϕ (4 and 5, respectively) which is connected to a wider spread of the wave function in the ϕ direction, where the full shape of the potential starts to play a role. As we can see in Fig. 6 where we show the 2D slice of $V(R = 1.88, \phi, \theta)$ and compare the constructed $\tilde{\Phi}_{(6)}$ with the true 2D Φ_6. The wave function 2D Φ_6 differs from $\tilde{\Phi}_{(6)}$ mainly in the first lobe which is somewhat broader and lower, which can be attributed trivially to "opening" of the potential at small values of ϕ. Nevertheless, this difference, although having rather small influence on the energy of the state (see Table III), does cause a non-negligible mixing with other states, as evidenced by the significant deviation of $\tilde{H}^{(full)}_{(6)(6)}$ from $\tilde{U}_{4,0}$. We also diagonalized the full Hamiltonian matrix evaluated over a basis of 400 states $\tilde{\Phi}_{\nu_\phi,\nu_\theta}$, with $\nu_\phi, \nu_\theta = 1, \ldots, 20$, and carried out the ten lowest eigenenergies $\tilde{E}^{(full)}_{(\nu)}$ in Table II. The correspondence between the eigenenergies and the real adiabatic 2D values indicates that the constructed states can be used as diabatic basis set.

Once the 2D basis functions $\tilde{\Phi}_{\nu_\phi,\nu_\theta}$ are constructed for the range of R of interest, we can trivially carry out the corresponding 1D $\tilde{U}_{\nu_\phi,\nu_\theta}(R)$. In particular, as shown in Fig. 7, the potential curves can be labeled as symmetric or antisymmetric in accordance with the even or odd quantum numbers ν_θ and with respect to the symmetry in the hyperangle θ.

B. Split of potential in θ and appearance of saddle

The OH + H dissociation limit along with the symmetry of the molecule leads to formation of a barrier at a particular size (or R) of the molecule when it begins to be energetically favorable for one of the hydrogen atoms to shift farther away from oxygen than the other. This twofold dissociation limit manifests trivially only in the γ set as the split of the potential minimum appears only in the hyperangle θ. The barrier arises at the hyperradius $R \approx 2.4$ as shown in Fig. 3.

The PES in the γ set manifests symmetry in the hyperspherical angle θ which is also preserved by the 1D wave

TABLE III. Projections $a_{i,(\nu)}$ at $R = 1.88$ a.u. Here the row number indicates the level order of the adiabatic state, and the column number is the order ν of the separable state (corresponding to the first column in Table II). The off-diagonal terms indicate the degree of coupling.

$i = \backslash\ (\nu) =$	(0)	(1)	(2)	(3)	(4)	(5)	(6)	(7)	(8)	(9)
0	0.999	0.025	0	0	0.001	0	0	0	0	0.007
1	0.026	0.997	0.032	0	0.002	0	0.003	0	0.001	0.034
2	0.001	0.038	0.993	0	0.035	0	0.005	0	0.006	0.012
3	0	0	0	0.996	0	0.075	0	0.003	0	0
4	0	0.002	0.049	0	0.987	0	0.033	0	0.012	0.004
5	0	0	0	0.079	0	0.985	0	0.098	0	0
6	0	0	0.004	0	0.060	0	0.976	0	0.025	0.001
7	0	0	0	0	0	0.115	0	0.970	0	0
8	0	0	0.001	0	0.007	0	0.073	0	0.959	0
9	0.010	0.037	0.020	0	0	0	0	0	0	0.989

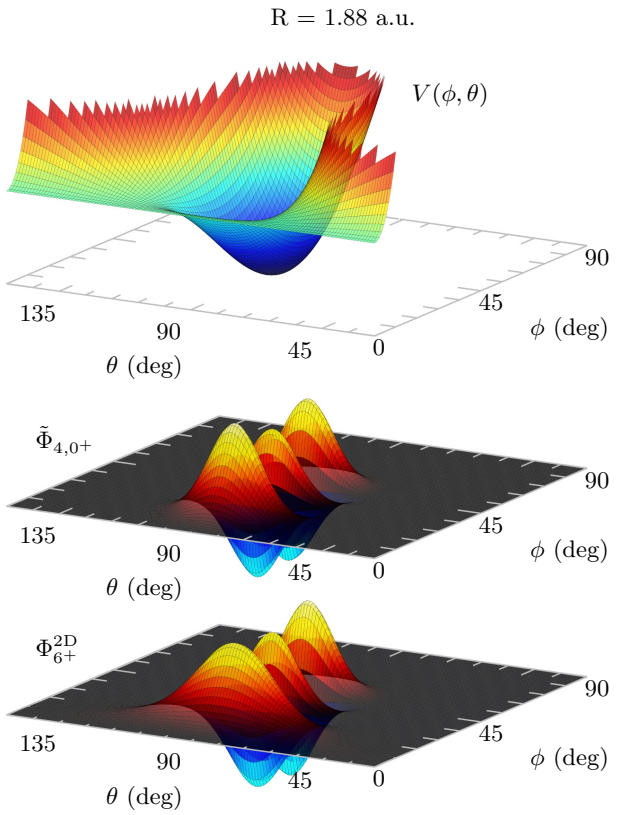

FIG. 6. Top panel: A slice of potential $V(R = 1.88, \phi, \theta)$. Comparison of the 2D adiabatic wave function (bottom panel) for the 7th state ($v = 6$) in Table II with the separable wave function (middle panel) for $\tilde{\Phi}_{4,0^+}$. The superscript + indicates the symmetry in the hyperspherical coordinate θ.

functions Θ_{v_θ} and the 1D potential $V(\theta) = V(R, \phi_{\min}, \theta) - V(R, \phi_{\min}, \theta_{\min})$. Therefore we can restrict our initial analysis to one dimension only. The formation of the barrier in the hyperangle θ is visualized in Fig. 8.

With increasing R the value of the minimum of the potential increases and a barrier at $\theta = 90^\circ$ starts to form. Moreover, the height of the barrier grows with the increasing hyperradius. As the height of the barrier increases, the energy difference between the neighboring states of opposite symmetry decreases till the states become degenerate at some point. The energies of lower-lying states converge to each other faster than the energies of higher-lying states, which is trivially understandable as the creation of two separate potential wells affects the lowest states mostly. We should note that only the states with opposite symmetry merge together. The rising of the potential barrier will affect the antisymmetric states less since they have a node at $\theta = 90^\circ$. For the symmetric states, as the potential barrier rises, the wave functions at and near $\theta = 90^\circ$ are in the classical forbidden region, thus with nonzero but very small probabilities. Therefore, the energy of the symmetric states will become very close to antisymmetric states since in both cases the wave functions in the barrier regions are both very small, resulting in the pair of symmetric and antisymmetric curves merging at large R where the potential barrier is high.

Now, we can understand why the two neighboring PECs of opposite symmetry merge together while staying separated from other PEC pairs of the same v_ϕ in Fig. 7 and what role is played by the barrier. In the top row of Fig. 9 we demonstrate how the barrier emerges in 2D. At equilibrium $R = 1.88$, as seen in the first potential surface in the top row, there is only one minimum in θ. Near $R = 2.5$, this minimum begins to split, where a saddle starts to form, and the two minima shift apart with increasing R, as shown for $R = 3$ [see Figs. 3(c)–3(d) for more details on the position of the minima]. In the remaining rows of Fig. 9, we show how the 2D $\tilde{\Phi}_{v_\phi, v_\theta}(\phi, \theta)$ wave functions evolve with R for three pairs of states where each pair becomes degenerate at large R. Before the saddle, the symmetric state lies much lower that the antisymmetric state, where the symmetric state has much larger probability distributions near the symmetry point $\theta = 90^\circ$. At the saddle, each wave function begins to spread and eventually the wave function splits into two distinct parts at $R = 3$. In doing so, the nodal structure at $\theta = 90^\circ$ remains the same. Since the barrier height increases with R, the large probability density for the symmetric state at $\theta = 90^\circ$ begins to diminish. For large R, the probability densities for symmetric and antisymmetric states in the barrier region both become very small, leading to two degenerate states at large R in each pair. Such "bifurcation" at the saddle occurs at increasing R as the vibrational energies of the states increase. For such degenerate states, the linear combination of the symmetric and antisymmetric states results in two localized states:

$$\tilde{\Phi}_{\mathrm{H+OH}} = \frac{\tilde{\Phi}_{0,0^+} + \tilde{\Phi}_{0,1^-}}{\sqrt{2}},$$
$$\tilde{\Phi}_{\mathrm{HO+H}} = \frac{\tilde{\Phi}_{0,0^+} - \tilde{\Phi}_{0,1^-}}{\sqrt{2}}. \quad (33)$$

These two localized states are related to either case of the attachment of one hydrogen atom to one oxygen atom with the other hydrogen atom far away. Figure 10 illustrates such cases at $R = 4$ a.u. In the top panels, we illustrate the 2D potential surface, highlighting where the potential wells are located in each set of Jacobi coordinates and the exact positions of the minima are marked by white crosses. For each localized state, the wave function is confined only to one narrow region, as clearly seen in each Jacobi set of hyperspherical angles illustrated in the middle and bottom panels.

Each linear combination represents the dissociation limit for different hydrogen atoms as indicated by the subscript. Such localization of the hyperspherical modes towards dissociation of one or the other hydrogen atom is possible only due to the energy degeneracy for symmetric and antisymmetric neighboring states. We should keep in mind that the degeneracy of the two neighboring states appears at a particular value of R which depends on their energy via quantum numbers v_ϕ and v_θ as discussed in Fig. 7.

Let us remark that the creation of energy-degenerate pairs at large hyperadii was also observed for the true 2D wave functions and is well reproduced in the present approach.

So far, we have developed a framework adiabatically connecting equilibrium vibrational states with dissociative vibrational states at large hyperradii. Intuitively, the most

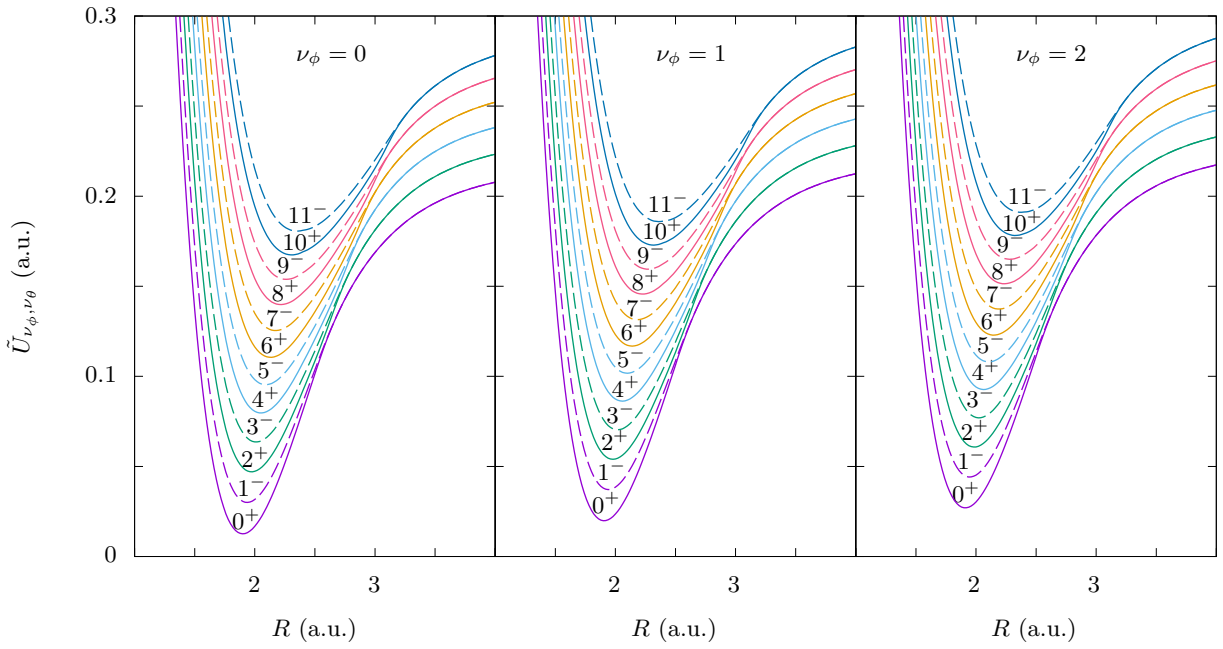

FIG. 7. Depiction of several lowest energies $\tilde{U}_{\nu_\phi=0,1,2;\nu_\theta}$ of the 2D states $\tilde{\Phi}_{\nu_\phi,\nu_\theta}$ constructed via the separation method. The PECs of the same ν_ϕ are separable without any crossings. The states symmetric in θ are shown by solid lines and marked with a superscript $+$, and the antisymmetric states are shown by dashed lines and a superscript $-$. The potential energy curves for states with opposite symmetry and $\nu_\theta = 2n - 2$ and $\nu_\theta = 2n - 1$ are shown with the same color. Each pair merges into a single curve at large R. As expected, the merging occurs at larger values of R with increasing quantum number ν_θ.

efficient control of dissociative products by ultrafast pulses is to manipulate these states in the transition region. Such knowledge would be invaluable for optimization of reaction products in the future.

V. CONSTRUCTION OF THE FULL VIBRATIONAL STATES

The full vibrational states can now be constructed via Eq. (14) using the PEC from Eq. (28). The correct procedure should involve also the nonadiabatic corrections as shown

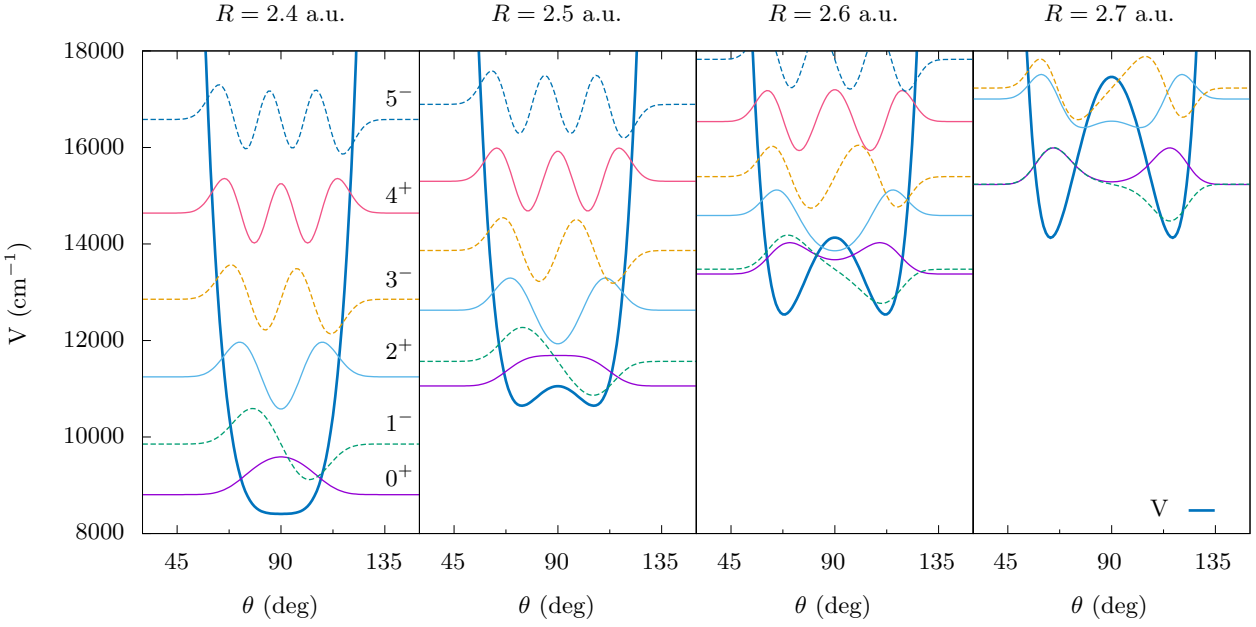

FIG. 8. Formation of the barrier in the molecular potential visualized as a 1D slice. The potential $V(\theta) = V(R, \phi_{\min}, \theta) - \frac{1}{2}V(R, \phi_{\min}, \theta_{\min})$ is shown as a thick blue line while low-lying states Θ_{ν_θ} are shown as thin colored lines. With increasing hyperradius R, a single potential well at small R will deform into two potential wells, separated by a growing potential barrier. As the barrier grows, the wave function of the symmetric state in the barrier region becomes very small; thus its energy becomes very close to the antisymmetric state, resulting in pairs of degenerate states at a large hyperradius. Note that the nodal structures of the wave functions do not change versus R.

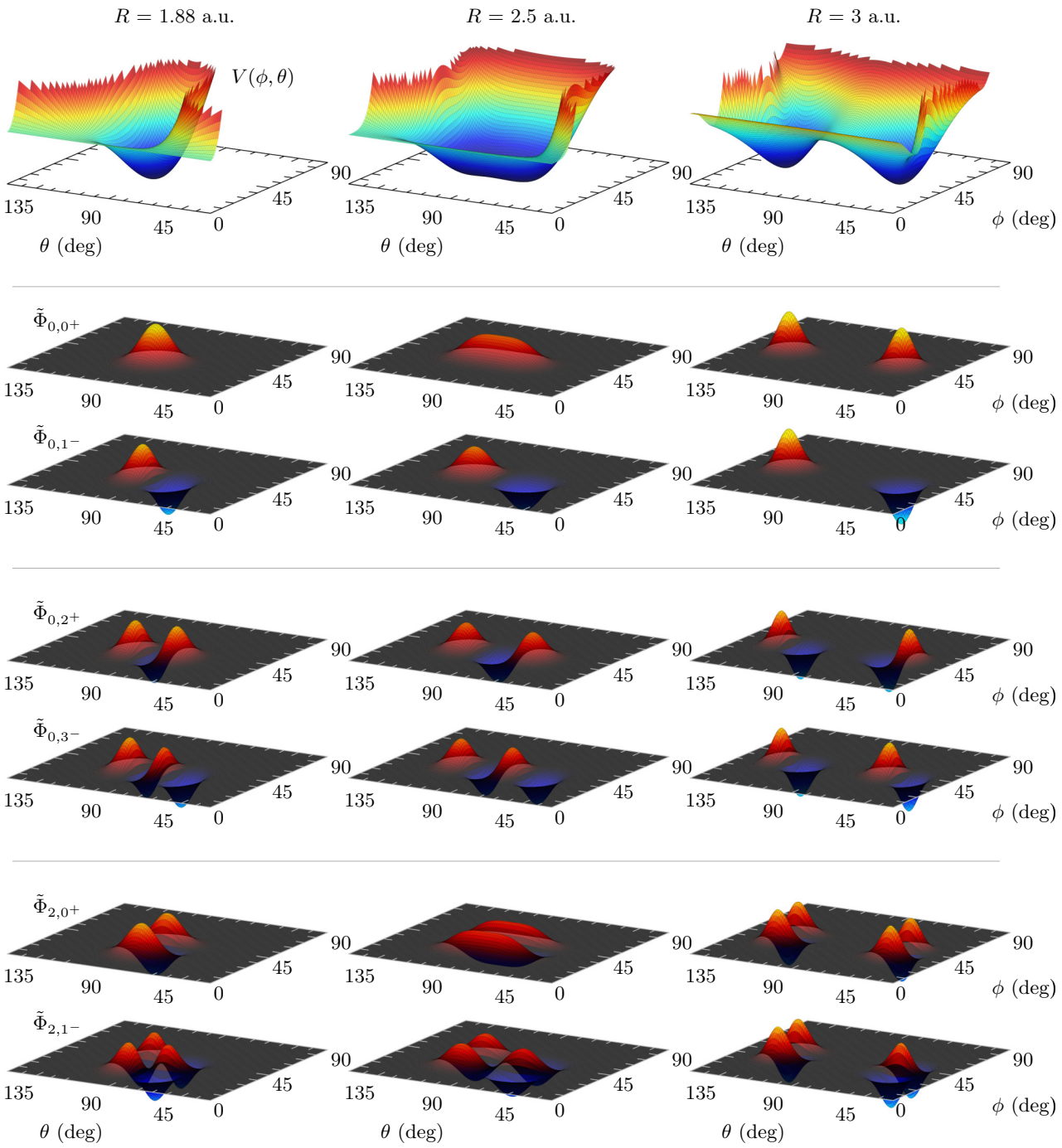

FIG. 9. We plotted three most distinct shapes of the PES slices with respect to the value of R on the first line. As we can see the 2D PES slices evolve from having one minimum ($R \lesssim 2.4$ a.u.) towards having two distinct minima ($R \gtrsim 2.4$ a.u.) separated by a saddlelike barrier with the height increasing with R. On the remaining lines we carried out the corresponding 2D functions $\tilde{\Phi}_{\nu_\phi,\nu_\theta}$ which we organized with respect to their symmetries in θ and energy degeneracy at large R. The deformation of the symmetric states due to the barrier is more severe than that of the antisymmetric states, leading to the creation of degenerate energy pairs as we already discussed for the 1D slices in the text.

in Eq. (16), but since our PEC was already evaluated in the separable approximation of the potential, it makes little sense to incorporate the relatively small nonadiabatic terms to increase the precision. Nevertheless, it is worth noting that the nonadiabatic correction terms peak at the split of the potential at $R \approx 2.4$ a.u., which is the place where the symmetric and antisymmetric states start to degenerate in energy.

For illustration we carried out the four lowest 1D solutions $F_{\nu_R}(R)$ on the lowest PEC $\tilde{U}_{\nu_\phi=0,\nu_\theta=0^+}(R)$ in Fig. 11. One could ask how precise are the energies $E_{\nu_R,\nu_\phi,\nu_\theta}$ after all these approximations are made. Interestingly, the computed energies are very precise for energies up to roughly 19 500 cm^{-1}. In this comparison, the data were obtained with optimized discrete variable representation calculated with dif-

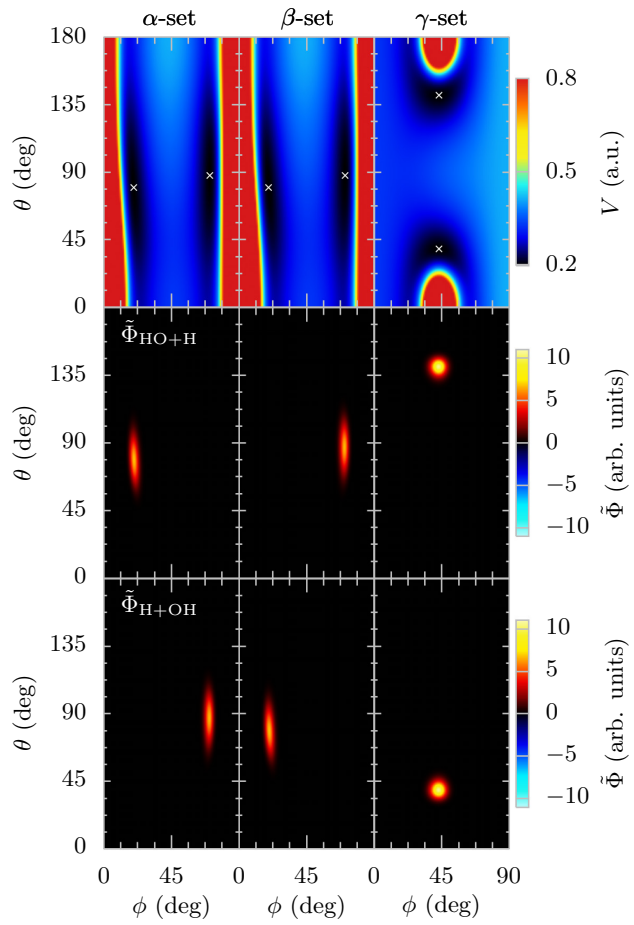

FIG. 10. Top row: 2D potential slice $V(\phi, \theta)$ at $R = 4$ a.u. for the three sets of hyperspherical coordinates. The dark blue regions indicate the potential wells with minima marked by white crosses separated by the saddle which looks different in each set. Middle and bottom rows: The localized wave functions given in Eq. (33). As we can see, each wave function is represented by a well-localized state, corresponding to the dissociation of a different hydrogen atom via the corresponding potential minimum.

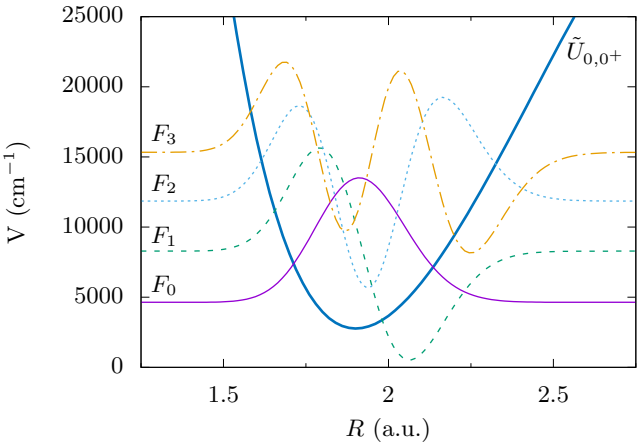

FIG. 11. The four lowest 1D solutions $F_n(R)$ to Eq. (14) with $\tilde{U}_{0,0^+}(R)$.

ferently defined hyperspherical coordinates but on the same PES in Ref. [30]. The zero-point energy we determined is 4635.14 cm^{-1}, as compared to the value of 4629.98 cm^{-1} given by Neto and Costa in Ref. [30], a difference of only 5.2 cm^{-1}.

Nevertheless, it is expected that the zero-point energy will be reproduced correctly as the ground state lies in the separability region and the nonadiabatic corrections are the smallest. As we have already mentioned, the approximation of separability introduces discrepancies for highly excited 2D states (e.g., $\Phi_{4,0^+}$) and therefore errors are expected to rise with increasing quantum state. To get a better picture of the errors introduced with the approximations we show a list of low-lying vibrational states labeled by the three quantum numbers which are readily available based on the separable approximate wave functions. The vibrational energy levels obtained from the present calculations are then compared to those given by Neto and Costa [30] in Table IV. The relative error of the calculated energies at most are about 2–3%, but mostly are under 1%.

As the largest source of discrepancy between the result presented here and in Ref. [30], we regard the breakdown of the potential semiseparability from Eqs. (29) in the two hyperangles for higher excitation states. We also found that inclusion of the diagonal nonadiabatic terms $W_{\nu\nu}(R)$ does not generally improve the results in Table IV.

VI. DISCUSSION

In this article we have addressed the separability of nuclear vibrational states in a water molecule in its electronic ground state in hyperspherical coordinates as an alternative to the well-known and somewhat complementary normal-mode and local-mode approaches. As the starting point, we applied adiabatic approximation in the hyperradius, separating it from the two hyperangles. Further simplification of the problem was motivated by the observed semiseparability in the 2D energy spectra and verified in the separation of the 2D problem into two independent 1D problems for each hyperangle. The presented framework was then used for the construction of adiabatic 1D PECs as functions of the hyperradius. Classification and separability of all adiabatic 1D PECs with respect to the underlying quantum numbers associated with the hyperangles was discussed. Pairwise degeneracy of two neighboring PECs of opposite symmetry at large values of hyperradius was observed and connected to formation of a saddlelike barrier associated with the twofold OH + H dissociation limit. The role of the barrier on the 2D vibrational states was thoroughly investigated and shape deformation followed by separation of symmetric states with increasing hyperradius was observed while the shape of antisymmetric states after separation remained unchanged. This not only explains the pairwise degeneracy of 1D PECs but also provides a possibility to control the dissociation process because which of the two hydrogen atoms will dissociate from the molecule will be determined by the linear combination of the paired 2D wave functions. A possible control scheme emerges as these states are adiabatically linked to specific vibrational states near equilibrium geometry.

TABLE IV. Comparing the determined energies with the highly precise values from Ref. [30].

v_R	v_ϕ	v_θ	$E^{(\mathrm{Neto})}$ (cm^{-1})	$E^{(\mathrm{pres.})}$ (cm^{-1})	Rel. diff. (%)
0	0	0	0	5.2	0.1
0	1	0	1594.2	1588.6	0.4
0	2	0	3151.7	3139.0	0.4
1	0	0	3656.1	3654.9	0.0
0	0	1	3755.6	3773.6	0.5
0	3	0	4667.3	4650.7	0.4
1	1	0	5233.8	5207.7	0.5
0	1	1	5331.6	5318.5	0.2
0	4	0	6133.7	6115.7	0.3
1	2	0	6774.5	6727.6	0.7
0	2	1	6872.9	6832.6	0.6
2	0	0	7202.1	7221.1	0.3
1	0	1	7250.3	7267.8	0.2
0	0	2	7444.4	7467.5	0.3
0	5	0	7539.4	7523.7	0.2
1	3	0	8272.6	8208.8	0.8
0	3	1	8375.0	8310.7	0.8
2	1	0	8762.2	8743.6	0.2
1	1	1	8808.9	8780.1	0.3
0	6	0	8862.8	8863.8	0.0
0	1	2	9001.4	8973.1	0.3
1	4	0	9719.1	9643.6	0.8
0	4	1	9832.0	9746.0	0.9
0	7	0	10073.4	10142.5	0.7
2	2	0	10284.9	10233.5	0.5
1	2	1	10331.6	10261.8	0.7
0	2	2	10524.8	10449.8	0.7
3	0	0	10601.9	10701.4	0.9
2	0	1	10614.8	10673.0	0.5
1	0	2	10868.5	10812.9	0.5
0	0	3	11033.3	11085.5	0.5
1	5	0	11081.7	11021.8	0.5
0	8	0	11234.4	11404.5	**1.5**
0	5	1	11234.6	11129.3	0.9
2	3	0	11765.3	11684.9	0.7
1	3	1	11814.6	11707.5	0.9
0	3	2	12010.7	11893.1	1.0
3	1	0	12143.5	12194.2	0.4
2	1	1	12155.6	12152.9	0.0
1	6	0	12341.5	12337.8	0.0
1	1	2	12407.5	12284.5	1.0
0	9	0	12504.5	12708.7	**1.6**
0	6	1	12566.5	12449.9	0.9
0	1	3	12570.5	12551.0	0.2
2	4	0	13194.9	13090.1	0.8
1	4	1	13251.7	13110.3	1.1
0	4	2	13452.8	13296.9	1.2
1	7	0	13605.4	13610.5	0.0
3	2	0	13646.8	13654.5	0.1
2	2	1	13657.7	13602.3	0.4
0	10	0	13796.7	14084.6	**2.0**
0	7	1	13798.7	13707.4	0.7
2	0	2	13828.7	14067.0	**1.7**
3	0	1	13831.0	13983.9	1.1
1	2	2	13910.7	13727.5	1.3
0	2	3	14075.0	13989.4	0.6
4	0	0	14222.4	14092.4	0.9
1	0	3	14320.5	14288.6	0.2
0	0	4	14540.4	14627.0	0.6
2	5	0	14548.3	14439.7	0.8
1	5	1	14629.4	14461.2	1.2
1	8	0	14778.4	14877.9	0.7
0	5	2	14858.3	14653.3	1.4
0	8	1	14932.6	14933.0	0.0
3	3	0	15108.6	15076.8	0.2
2	3	1	15121.5	15016.0	0.7
0	11	0	15190.2	15530.1	**2.2**
2	1	2	15349.1	15505.1	1.0
3	1	1	15354.2	15431.9	0.5
1	3	2	15376.0	15137.0	**1.6**
0	3	3	15544.2	15396.6	1.0
4	1	0	15742.9	15556.6	1.2
2	6	0	15809.5	15732.3	0.5
1	1	3	15838.0	15719.2	0.8
1	6	1	15922.4	15753.0	1.1
1	9	0	16024.7	16171.2	0.9
0	1	4	16056.5	16051.6	0.0
0	9	1	16109.4	16182.3	0.5
0	6	2	16186.4	15952.3	**1.5**
3	4	0	16524.3	16453.4	0.4
2	4	1	16540.1	16387.0	0.9
0	12	0	16670.8	17031.4	**2.1**
1	4	2	16783.2	16506.9	**1.7**
3	2	1	16822.8	16849.8	0.2
2	2	2	16825.1	16914.8	0.5
3	0	2	16898.8	17225.7	**1.9**
2	0	3	16898.6	17398.6	**2.9**
0	4	3	16973.6	16767.3	1.2
2	7	0	17055.7	16992.3	0.4
1	7	1	17157.0	16996.9	0.9
4	2	0	17224.9	16988.9	1.4
1	10	0	17316.5	17515.0	1.1
1	2	3	17319.1	17123.0	1.1
0	10	1	17378.6	17493.1	0.7
0	7	2	17434.5	17189.0	1.4
5	0	0	17460.0	17386.9	0.4
4	0	1	17495.9	17192.9	**1.8**
0	2	4	17541.3	17450.9	0.5
1	0	4	17753.6	17693.6	0.3
3	5	0	17876.8	17775.4	0.6
2	5	1	17902.1	17706.6	1.1
1	5	2	18120.0	17829.3	**1.6**
0	13	0	18194.7	18574.6	**2.0**
2	8	0	18260.0	18251.8	0.0
2	3	2	18273.1	18291.3	0.1
1	11	0	18695.7	18920.5	1.2
5	1	0	18957.7	18826.0	0.7
0	3	4	18994.9	18820.9	0.9
3	6	0	19147.8	19044.6	0.5
1	1	4	19249.7	19083.1	0.9
1	6	2	19377.1	19096.0	**1.5**
2	9	0	19493.2	19530.8	0.2
2	4	2	19664.8	19628.5	0.2
0	9	2	19697.5	19581.5	0.6

TABLE IV. (*Continued.*)

Finally, we have tested the validity of our framework by constructing the full 3D vibrational states within the adiabatic and separability approximation. The resulting energies yield an amazing correspondence to the high precision 3D calculations and differ maximally by 2.9% for the values up to 19 500 cm^{-1}.

Among the undeniable advantages of the presented framework we count the simplicity of vibrational state construction reducing the generally nontrivial 3D problem into three trivial 1D problems while yielding reasonably precise energies with only small deviations from the exact values. Let us note that the assignment and interpretation of vibrational quantum numbers in a full numerical 3D calculation can be very challenging especially when an unsuitable coordinate system is used. Nevertheless, the construction procedure presented here gives rise naturally to the vibrational quantum numbers which are easily understandable in the context of the separated hyperspherical modes.

It is also fair to mention that the present approach is not aimed at high-precision calculation of vibrational energy levels. Whether the approximate separability demonstrated here for water molecules can be extended to other molecular systems remains to be studied further. It is interesting to note that at least the separable vibrational wave functions constructed in this paper would serve as convenient diabatic basis functions for scattering calculations, thus replacing the complicated nonadiabatic couplings at multidimensional conical intersections with residual interactions from the potential surfaces that were neglected in the separable one-dimensional potentials.

To conclude, it is fair to say that there still remains a lot to be done. How the simplified framework of treating multidimensional nuclear dynamics can indeed be utilized to predict realistic laser-induced molecular dynamics as well as to provide simple interpretation of the underlying mechanism has yet to be demonstrated. Without taking such a step, on the other hand, it is difficult to expect that one can indeed understand the dynamics for a complex molecule.

ACKNOWLEDGMENTS

This research was supported in part by the Chemical Sciences, Geosciences, and Biosciences Division, Office of Basic Energy Sciences, Office of Science, U.S. Department of Energy, under Grant No. DE-FG02-86ER13491.

APPENDIX: ATOMIC DISPLACEMENTS IN THE γ SET

The positions of the hydrogen atoms $\mathbf{R}_1$ and $\mathbf{R}_2$ and the center of mass of the molecule $\mathbf{R}_{CM}$ are shown in Fig. 12 and the vectors can be linked to the Jacobi vectors as follows:

$$\begin{aligned}\mathbf{R}_1 &= -\boldsymbol{\rho}_2 - \tfrac{\mu_1}{m_H}\boldsymbol{\rho}_1 = -\boldsymbol{\rho}_2 - \frac{\boldsymbol{\rho}_1}{2},\\ \mathbf{R}_2 &= -\boldsymbol{\rho}_2 + \tfrac{\mu_1}{m_H}\boldsymbol{\rho}_1 = -\boldsymbol{\rho}_2 + \frac{\boldsymbol{\rho}_1}{2},\\ \mathbf{R}_{CM} &= \tfrac{m_O}{2m_H+m_O}\boldsymbol{\rho}_2 \quad = \frac{\mu_2}{4\mu_1}\boldsymbol{\rho}_2.\end{aligned} \tag{A1}$$

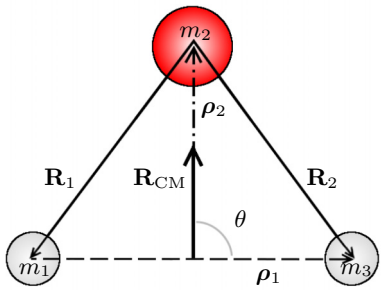

FIG. 12. Definition of Jacobi vectors $\boldsymbol{\rho}_1$ and $\boldsymbol{\rho}_2$ and their mutual angle θ in the γ set and the molecular bond vectors $\mathbf{R}_1$ and $\mathbf{R}_2$. The center-of-mass of the whole molecule is located at $\mathbf{R}_{CM}$.

The size of the Jacobi vectors is related to the hyperspherical coordinates R and ϕ via

$$\rho_1 = \sqrt{\frac{\mu}{\mu_1}}\frac{R}{\sqrt{1+\tan^2\phi}}, \quad \rho_2 = \sqrt{\frac{\mu}{\mu_2}}\frac{R\tan\phi}{\sqrt{1+\tan^2\phi}}. \tag{A2}$$

The variables ρ_1 and ρ_2 are interconnected with respect to derivation:

$$\begin{aligned}\frac{d\rho_1}{dR} &= \frac{\rho_1}{R}, \qquad \frac{d\rho_1}{d\phi} = -\sqrt{\frac{\mu_2}{\mu_1}}\rho_2,\\ \frac{d\rho_2}{dR} &= \frac{\rho_2}{R}, \qquad \frac{d\rho_2}{d\phi} = +\sqrt{\frac{\mu_1}{\mu_2}}\rho_1.\end{aligned} \tag{A3}$$

It is possible to show that

$$\begin{aligned}\frac{\mathbf{R}_{1,2}\cdot\partial_R\mathbf{R}_{1,2}}{|\mathbf{R}_{1,2}||\partial_R\mathbf{R}_{1,2}|} &= 1,\\ \frac{\tilde{\mathbf{R}}_{1,2}\cdot\partial_R\tilde{\mathbf{R}}_{1,2}}{|\tilde{\mathbf{R}}_{1,2}||\partial_R\tilde{\mathbf{R}}_{1,2}|} &= 1,\end{aligned} \tag{A4}$$

where $\tilde{\mathbf{R}}_{1,2} = \mathbf{R}_{1,2} - \mathbf{R}_{CM}$. Neither of the remaining displacement vectors $\partial_\phi\mathbf{R}_{1,2}$, $\partial_\phi\tilde{\mathbf{R}}_{1,2}$, $\partial_\theta\mathbf{R}_{1,2}$, and $\partial_\theta\tilde{\mathbf{R}}_{1,2}$ is generally parallel or perpendicular to the vector $\mathbf{R}_{1,2}$ or $\tilde{\mathbf{R}}_{1,2}$ and their mutual angles are given by rather complicated and not very enlightening relations, depending only on angles ϕ and θ and on masses μ_1, μ_2, and μ. The displacement vectors with respect to individual coordinates can be at equilibrium, i.e.,

TABLE V. Character table for the normal modes (ν_1, ν_2, ν_3) and the hyperspherical modes (ν_R, ν_ϕ, ν_θ) of a water molecule.

C_{2v}	E	C_2	$\sigma(xy)$	$\sigma(yz)$
ν_1	1	1	1	1
ν_2	1	1	1	1
ν_3	1	−1	−1	1
ν_R	1	1	1	1
ν_ϕ	1	1	1	1
ν_θ	1	−1	−1	1

$\theta = 90^\circ$, expressed for the change in the hyperradius R as

$$\begin{aligned}\partial_R \mathbf{R}_1 &= \frac{1}{2R}\left(-\rho_1,\ 0,\ -2\rho_2\right),\\ \partial_R \mathbf{R}_2 &= \frac{1}{2R}\left(+\rho_1,\ 0,\ -2\rho_2\right),\\ \partial_R \mathbf{R}_{\rm CM} &= \frac{\mu_2\rho_2}{4\mu_1 R}(0,\ 0,\ 1),\end{aligned} \tag{A5}$$

in the hyperangle ϕ as

$$\begin{aligned}\partial_\phi \mathbf{R}_1 &= \left(+\sqrt{\frac{\mu_2}{\mu_1}}\frac{\rho_2}{2},\ 0,\ -\sqrt{\frac{\mu_1}{\mu_2}}\rho_1\right),\\ \partial_\phi \mathbf{R}_2 &= \left(-\sqrt{\frac{\mu_2}{\mu_1}}\frac{\rho_2}{2},\ 0,\ -\sqrt{\frac{\mu_1}{\mu_2}}\rho_1\right),\\ \partial_\phi \mathbf{R}_{\rm CM} &= \sqrt{\frac{\mu_2}{\mu_1}}\frac{\rho_1}{4}(0,\ 0,\ 1),\end{aligned} \tag{A6}$$

and in hyperangle θ as

$$\begin{aligned}\partial_\theta \mathbf{R}_1 &= \frac{\rho_1}{2}(0,\ 0,\ +1),\\ \partial_\theta \mathbf{R}_2 &= \frac{\rho_1}{2}(0,\ 0,\ -1),\\ \partial_\theta \mathbf{R}_{\rm CM} &= \frac{\mu_2\rho_2}{4\mu_1}(0,\ 0,\ 1).\end{aligned} \tag{A7}$$

The upper results at the equilibrium can be used to construct the character table of the displacements and those can be compared with the character table for the normal modes (see Table V).

Nevertheless, displacement in the individual hyperspherical coordinates are strictly speaking not the well-known normal modes since the kinetic part of the Hamiltonian in Eq. (9) is not separable in the hyperangular part.

[1] A. Trabattoni, M. Klinker, J. González-Vázquez, C. Liu, G. Sansone, R. Linguerri, M. Hochlaf, J. Klei, M. J. J. Vrakking, F. Martín, M. Nisoli, and F. Calegari, Mapping the Dissociative Ionization Dynamics of Molecular Nitrogen with Attosecond Time Resolution, Phys. Rev. X **5**, 041053 (2015).

[2] F. Krausz and M. Ivanov, Attosecond physics, Rev. Mod. Phys. **81**, 163 (2009).

[3] M. Nisoli, P. Decleva, F. Calegari, A. Palacios, and F. Martín, Attosecond electron dynamics in molecules, Chem. Rev. **117**, 10760 (2017).

[4] W. Demtröder, *Atoms, Molecules and Photons* (Springer, Berlin, 2006).

[5] L. Halonen and T. Carrington, Fermi resonances and local modes in water, hydrogen sulfide, and hydrogen selenide, J. Chem. Phys. **88**, 4171 (1988).

[6] B. T. Darling and D. M. Dennison, The water vapor molecule, Phys. Rev. **57**, 128 (1940).

[7] K. Kuchitsu and L. S. Bartell, Effect of anharmonic vibrations on the bond lengths of polyatomic molecules. I. Model of force field and application to water, J. Chem. Phys. **36**, 2460 (1962).

[8] M. S. Child and L. Halonen, *Overtone Frequencies and Intensities in the Local Mode Picture* (Wiley & Sons, New York, 2007), pp. 1–58.

[9] M. Carleer, A. Jenouvrier, A.-C. Vandaele, P. F. Bernath, M. F. Mérienne, R. Colin, N. F. Zobov, O. L. Polyansky, J. Tennyson, and V. A. Savin, The near infrared, visible, and near ultraviolet overtone spectrum of water, J. Chem. Phys. **111**, 2444 (1999).

[10] S. E. Choi and J. C. Light, Highly excited vibrational eigenstates of nonlinear triatomic molecules. Application to H_2O, J. Chem. Phys. **97**, 7031 (1992).

[11] J. Manz and H. Schor, Hyperspherical modes, Chem. Phys. Lett. **107**, 542 (1984).

[12] A. Bastida, J. Zúlñiga, A. M. Molina, and A. Requena, Vibrational self-consistent-field approximation for triatomic molecules using hyperspherical modes with application to H_2O, Int. J. Quantum Chem. **42**, 475 (1992).

[13] T. Joseph, T.-M. Kruel, J. Manz, and I. Rexrodt, Model calculation of local versus hyperspherical mode selective dissociation of H_2O, Chem. Phys. **113**, 223 (1987).

[14] B. Hartke, J. Manz, and J. Mathis, Mode selective control of unimolecular dissociations: Survey, and model simulations for HDO → H+DO, D+HO, Chem. Phys. **139**, 123 (1989).

[15] B. Hartke and J. Manz, A new quantum isotope effect: Extreme local mode selectivity in unimolecular dissociations imposed by antagonism between dynamic propensities of educts and zero point energies of products, J. Chem. Phys. **92**, 220 (1990).

[16] B. Hartke, A. E. Janza, W. Karrlein, J. Manz, V. Mohan, and H. Schreier, Local versus hyperspherical modes of water and formaldehyde: Effect of molecular complexity on mode-selective structures and dynamics, J. Chem. Phys. **96**, 3569 (1992).

[17] B. R. Johnson and W. P. Reinhardt, Adiabatic separations of stretching and bending vibrations: Application to H_2O, J. Chem. Phys. **85**, 4538 (1986).

[18] B. J. Rosenberg, W. C. Ermler, and I. Shavitt, *Ab initio* SCF and CI studies on the ground state of the water molecule. II. Potential energy and property surfaces, J. Chem. Phys. **65**, 4072 (1976).

[19] A. J. Dobbyn and P. J. Knowles, A comparative study of methods for describing non-adiabatic coupling: Diabatic representation of the 1Sigma +/1Pi HOH and HHO conical intersections, Mol. Phys. **91**, 1107 (1997).

[20] R. van Harrevelt and M. C. van Hemert, Photodissociation of water. I. Electronic structure calculations for the excited states, J. Chem. Phys. **112**, 5777 (2000).

[21] O. L. Polyansky, A. G. Császár, S. V. Shirin, N. F. Zobov, P. Barletta, J. Tennyson, D. W. Schwenke, and P. J. Knowles, High-accuracy ab initio rotation-vibration transitions for water, Science **299**, 539 (2003).

[22] P. Barletta, S. V. Shirin, N. F. Zobov, O. L. Polyansky, J. Tennyson, E. F. Valeev, and A. G. Császár, CVRQD *ab initio* ground-state adiabatic potential energy surfaces for the water molecule, J. Chem. Phys. **125**, 204307 (2006).

[23] S. V. Shirin, N. F. Zobov, R. I. Ovsyannikov, O. L. Polyansky, and J. Tennyson, Water line lists close to experimental accuracy using a spectroscopically determined potential energy surface for $H_2{}^{16}O$, $H_2{}^{17}O$, and $H_2{}^{18}O$, J. Chem. Phys. **128**, 224306 (2008).

[24] I. I. Bubukina, N. F. Zobov, O. L. Polyansky, S. V. Shirin, and S. N. Yurchenko, Optimized semiempirical potential energy surface for $H_2{}^{16}O$ up to 26000 cm^{-1}, Opt. Spectrosc. **110**, 160 (2011).

[25] B. Jiang, D. Xie, and H. Guo, Communication: State-to-state differential cross sections for $H_2O(B)$ photodissociation, J. Chem. Phys. **134**, 231103 (2011).

[26] B. Jiang, D. Xie, and H. Guo, State-to-state photodissociation dynamics of triatomic molecules: H_2O in the B band, J. Chem. Phys. **136**, 034302 (2012).

[27] O. L. Polyansky, A. A. Kyuberis, N. F. Zobov, J. Tennyson, S. N. Yurchenko, and L. Lodi, ExoMol molecular line lists XXX: a complete high-accuracy line list for water, Mon. Not. R. Astron. Soc. **480**, 2597 (2018).

[28] P. Jensen, The potential energy surface for the electronic ground state of the water molecule determined from experimental data using a variational approach, J. Mol. Spectrosc. **133**, 438 (1989).

[29] C. D. Lin, Hyperspherical coordinate approach to atomic and other Coulombic three-body systems, Phys. Rep. **257**, 1 (1995).

[30] J. J. S. Neto and L. S. Costa, Numerical generation of optimized discrete variable representations, Braz. J. Phys. **28**, 1 (1998).

[31] J. Tennyson and B. T. Sutcliffe, The *ab initio* calculation of the vibrational-rotational spectrum of triatomic systems in the close-coupling approach, with KCN and H_2Ne as examples, J. Chem. Phys. **77**, 4061 (1982).

[32] C.-N. Liu, A.-T. Le, T. Morishita, B. D. Esry, and C. D. Lin, Hyperspherical close-coupling calculations for charge-transfer cross sections in $He^{2+} + H(1s)$ collisions at low energies, Phys. Rev. A **67**, 052705 (2003).

[33] A. Hoy, I. Mills, and G. Strey, Anharmonic force constant calculations, Mol. Phys. **24**, 1265 (1972).

[34] A. F. Starace and G. L. Webster, Atomic hydrogen in a uniform magnetic field: Low-lying energy levels for fields below 10^9 g, Phys. Rev. A **19**, 1629 (1979).

[35] B. D. Esry, C. D. Lin, and C. H. Greene, Adiabatic hyperspherical study of the helium trimer, Phys. Rev. A **54**, 394 (1996).

[36] H. Bachau, E. Cormier, P. Decleva, J. E. Hansen, and F. Martín, Applications of B-splines in atomic and molecular physics, Rep. Prog. Phys. **64**, 1815 (2001).